Thermal calibration of the MEDA-TIRS radiometer onboard NASA's Perseverance rover

Eduardo Sebastián[1], German Martínez[2,3], Miguel Ramos[4], Isabel Pérez-Grande[5], Jesús Sobrado[1], José A. Rodríguez[1].

[1]Departamento de Instrumentación Espacial, Centro de Astrobiología (CSIC-INTA), Torrejón de Ardoz, Madrid, Spain, sebastianme@cab.inta-csic.es
[2]Lunar and Planetary Institute/USRA, Houston, TX, USA
[3]Department of Climate and Space Sciences and Engineering, University of Michigan, Ann Arbor, MI, USA
[4]Departamento Física y Matemáticas, Universidad de Alcalá, Alcalá de Henares, Madrid, Spain
[5]Instituto de Microgravedad Ignacio Da Riva, Universidad Politécnica de Madrid, Madrid, Spain

Abstract

This article describes a comprehensive testing method for the thermal calibration of the Thermal InfraRed Sensor (TIRS) onboard NASA's *Perseverance* rover. Ground-based IR detectors operating at the surface of Mars are subjected to inaccuracies caused by the inclusion of thermal gradients in their packages. To reduce such uncertainties, it is necessary to compensate for their effects. Here, details of the TIRS thermo-mechanical design and a simplified thermal mathematical model (TMM) that accounts for the presence of thermal gradients in the detector's package are provided. Then, a set of equations for the estimation and compensation of thermal gradients are proposed based on the results of the TMM. Thermal calibration tests to identify the mathematical estimators are analyzed, providing details of the test setups and highlighting their limitations and restrictions. Finally, experimental results of the calibration tests are presented, along with the uncertainty sources and potential systematic errors associated with the estimation of the gradients. The results presented here show a significant improvement in the accuracy of TIRS versus previous work, thus fulfilling of the radiometer scientific requirements set by the Mars 2020 science team.

Keywords
Spacecraft IR radiometer, IR detector package gradients, Detector modeling, Thermal calibration, Calibration accuracy

1. Introduction

Among the different scientific instruments onboard NASA's Mars2020 Perseverance rover, the suit of sensors making up the Mars Environmental Dynamic Analyzer (MEDA) instrument was selected to characterize the environment in preparation for the human exploration of Mars, which is one of the four objectives of the M2020 mission [1]. MEDA's specific objectives are to characterize the atmospheric dust size and morphology to understand its effects on the operation of surface systems and human health, and to validate global atmospheric models by performing surface weather measurements. The in-situ meteorological measurements that will be collected by MEDA (air and ground temperature, radiative fluxes, wind speed and direction, pressure, and relative humidity) [2], together with the data collected by previous landing missions [3, 4], will expand our current understanding of the near-surface environmental conditions on Mars. These data are complementary to those obtained from Mars orbiters, which cannot resolve the atmospheric layers closest to the surface where rovers and landers operate [5]. A good characterization of the environment at surface level is also relevant to determine the presence of certain compounds as well as the cycle of water and forms of life [4]. Despite the vast amount of Mars surface data already available, there are still many strategic knowledge gaps that can only be closed by sending new missions to our neighbor planet [5]. Specifically,

the MEDA *in-situ* space radiometer called the Thermal Infrared Sensor (TIRS) [6] (Fig. 1) is used for the validation of atmospheric models by measuring the net thermal infrared, solar reflected radiation and atmosphere and ground temperature at the surface, through different channels and measurement bands (Table 1).

Channel	Purpose	Range[μm]	Pointing angles
IR1	Downward LW flux	6.5-30	Upward (+35º)
IR2	Atmosphere temperature	14.5-15.5	Upward (+35º)
IR3	Reflected SW	0.3-3	Downward (-35º)
IR4	Upward LW flux	6.5-30	Downward (-35º)
IR5	Surface brightness temperature	8-14	Downward (-35º)

Table 1. TIRS channels.

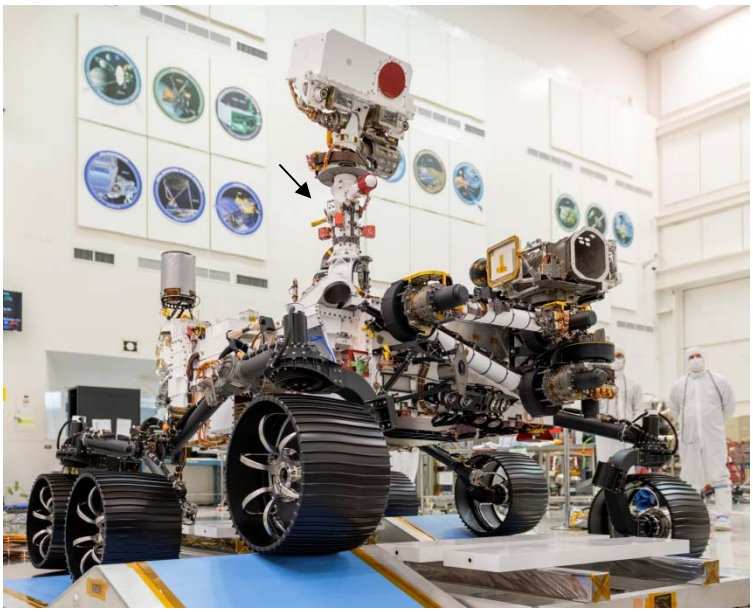

Figure 1. MEDA-TIRS located at NASA Perseverance rover remote sensing mast (black arrow, credit NASA-JPL).

One of the most important sources of uncertainty in infrared (IR) radiometry is the appearance of spatial thermal gradients in the package of the IR detectors [7, 8, 9, 10]. Therefore, a proper calibration of these gradients represents a key aspect to obtain reliable data. The main purpose of this article is to describe a comprehensive method for the compensation and calibration of the thermal gradients on the packages of the IR detectors. This calibration is part of the TIRS' calibration plan, whose general structure, test objectives and execution time frame are shown in (Fig. 2). Radiometric and angular calibration [11] tests have already been described in [12], while in-flight calibration tests will be discussed in forthcoming articles.

Section 2 of this article updates the description and justifies the final thermo-mechanical design of the TIRS flight model (FM), preliminarily presented for an engineering model in [6]. Additional information about isolation and fixing elements, optical treatments, and heater details is also provided. Section 3 includes a simplified mathematical model for the IR detectors, accounting for the existence of the package's internal thermal gradients. While this model was presented in [12], it is here modified to match the experimental setup used in the thermal calibration tests. Section 4 describes the TIRS Thermal Mathematical Model (TMM) [13] used to define a set of theoretical-practical equations, both steady-state and transient, that allow for the estimation of the package's internal thermal gradients. Section 5 presents a detailed description of the calibration procedure, test setups carried out with the TIRS FM inside a simulation chamber, and a critical discussion of the results. Section 6 analyzes the different sources of uncertainty and potential systematic errors associated with the gradients estimation. They are used to compute a global

uncertainty figure for the spatial thermal gradients (section 6), which supersedes the preliminary one provided in (Table 4) of [6]. Finally, Section 7 shows the conclusions.

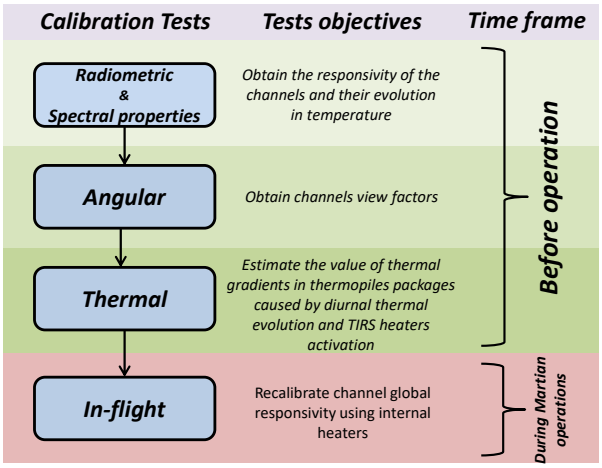

Figure 2. General view of the TIRS calibration plan

2. TIRS thermal design and detector gradients

Spatial thermal gradients in the sealed housing or package of the IR detectors arise as a result of operating in open-air applications [9], where detectors are subjected to sun irradiance [7] and wind gusts, or in applications where the entire radiometer structure is heated by an active thermal control system [8, 10, 14]. During Martian operations, the TIRS will have to operate in a thermally challenging environment. The rover Remote Sensing Mast (RSM), where the TIRS is located, is typically warmer than the Martian environment because of the rover's thermal control system. Also, the TIRS will be subjected to strong diurnal and seasonal thermal cycles, direct sun incidence and wind gusts. Thus, TIRS detectors are subject to thermal gradients on packages and these will condition the accuracy of the radiometer depending on different factors such as target view factor and filter bandpass. Thus, the narrower the filter bandpass and the smaller the target view factor, the smaller is the signal to noise ratio [15].

In high performance systems, and especially for channels with narrow band pass filters, the most widely used means of dealing with detector thermal gradients are mechanical choppers [8]. Nevertheless, choppers require the use of mechanical actuators [16], which reduce instrument robustness and increase its energy demands and overall risk of failure. Therefore, the use of choppers is undesirable [17] for *in-situ* space radiometers. Another technical solution to thermal gradients relies on the use of active thermal control systems (cooling or warming) [8, 10, 14, 18] These systems can minimize the thermal gradients, although they introduce additional mass, power consumption and volume. Usually, they also resort to computing mechanisms to compensate for detectors' readout voltage residuals caused by the thermal gradients not completely eliminated [8, 10].

The thermal design of the TIRS is mainly oriented toward the minimization of the thermopile packages' thermal gradients, by using a passive thermal control system [6]. In addition to this, an off-line computing system will be used to directly estimate and compensate for the thermal gradients. The approach follow in this compensation represents an advantage compared to other proposed solutions, where the variable compensated is the detector readout voltage [7, 9, 10]. Thermal gradients are independent of thermopile responsivity variations, but detector readout voltage is also affected by thermopile responsivity changes, and therefore the particular value of thermopile responsivity should be taken into account in the compensation.

The MEDA's Instrument Control Unit (ICU), where the TIRS electronic conditioning board is located, is away from the sensor head and connected through a 3-4m long harness. In this way, the thermal control to keep the electronic conditioning system within its operational temperature does not thermally disturb the IR detectors, avoiding the problem of the self-heating of amplification electronics and the consequent appearance of gradients described in [10].

From a thermo-mechanical point of view, the TIRS sensor head housing consists of an external aluminum structure and two fiberglass (FR4) covers, front and back (Fig.3a and b). This enclosure provides a mechanical chassis to fix to the Perseverance rover RSM and protect and insulate the IR detectors from the Martian environment. The external surfaces are painted using the MAP® SG121 white paint, with low absorptance (≈0.2), to reduce the solar heat loads. All the internal surfaces of the instrument have a low emissivity finish (≈0.08) [12], which is characteristic of the chromate conversion Alodine 1200 treatment (Fig.3c, d, e, and f) thereby reducing the radiative coupling between the support plate and the rest of the instrument.

The TIRS makes use of an almost isothermal mass, called support plate (Fig. 3c). This mass is located around the thermopiles' housing to minimize the thermal gradients and allow in-flight calibration [6]. The thermopiles are glued inside the support plate sub-assembly, using cryogenic thermal glue MASTERBOND® EP21TCHT-1 (Fig. 3e). The support plate subassembly is formed by two mechanical pieces made of aluminum that form a "sandwich" (Fig. 3f), which are conductively insulated from the housing using low thermal conductivity spacers made of FR4 and a flex-rigid PCB for electrical connection (Fig. 3a and g). Two Pt1000-type Resistance Temperature Detectors (RTDs) glued to the rear and front mechanical structures (Fig. 4e and f), to measure their corresponding temperatures T_{sp} and T_{sp_f}. Since it is closer to the thermopiles' package the one RTD located at the rear subassembly is intended to provide the IR detectors with temperature reference measurements (T_s=T_{sp}). Due to their different locations, there are exceedingly small differences in the measured temperatures, around tens of mK. Nevertheless, this difference cannot be used to estimate and compensate for the IR detector package's thermal gradients because of measurement resolution. Contrary to similar designs [14, 18], the support plate includes heaters only for in-flight calibration purposes, but not for thermal control of the detector's temperature (thus reducing the total energy consumption). *Kapton* film heaters are glued to the lateral side and are capable of providing up to 0.8W, Fig 3a and g. Heater power is determined by a PI controller and a Pulse Widthe Modulator (PWM) driver, with the goal of keeping the support plate temperature stable and above ambient temperature during in-flight calibration mode.

The calibration plate (Fig. 3d), is also made of aluminum. The plate has holes to conform the detectors FoV [6]. It acts as an in-flight calibration target, contributing to the signal seen at the detector only around the periphery of the detector FoV. It induces a known signal in the detectors by making use of two *Kapton* heaters of 0.8W commanded on/off and by measuring its temperature (T_{cp}) with a RTD-Pt1000 contact sensor. The area of the calibration plate inner face looking at the thermopiles presents an inorganic black anodized surface treatment, increasing its IR emissivity above 0.9 [12]. The calibration plate is attached to the housing front cover, helping to reduce the conductive coupling between the calibration plate and the rest of the sensor.

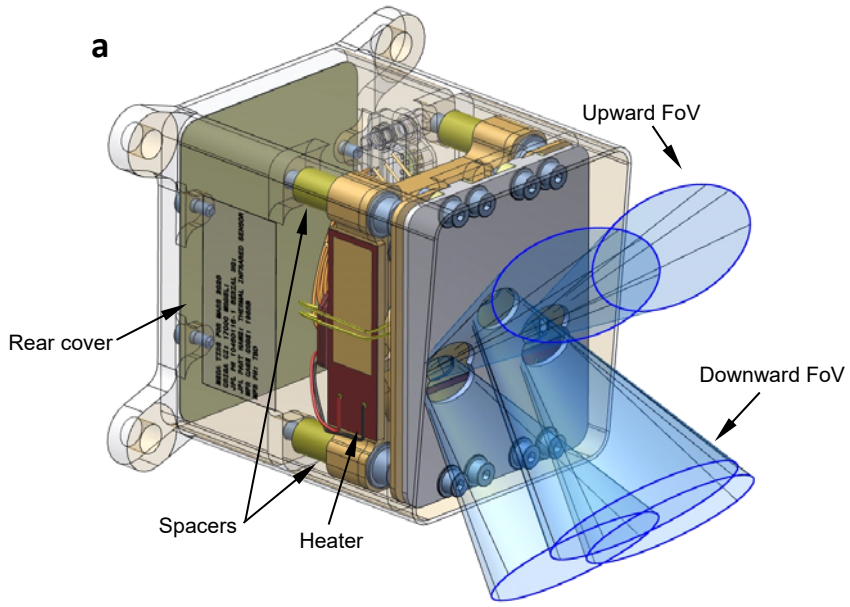

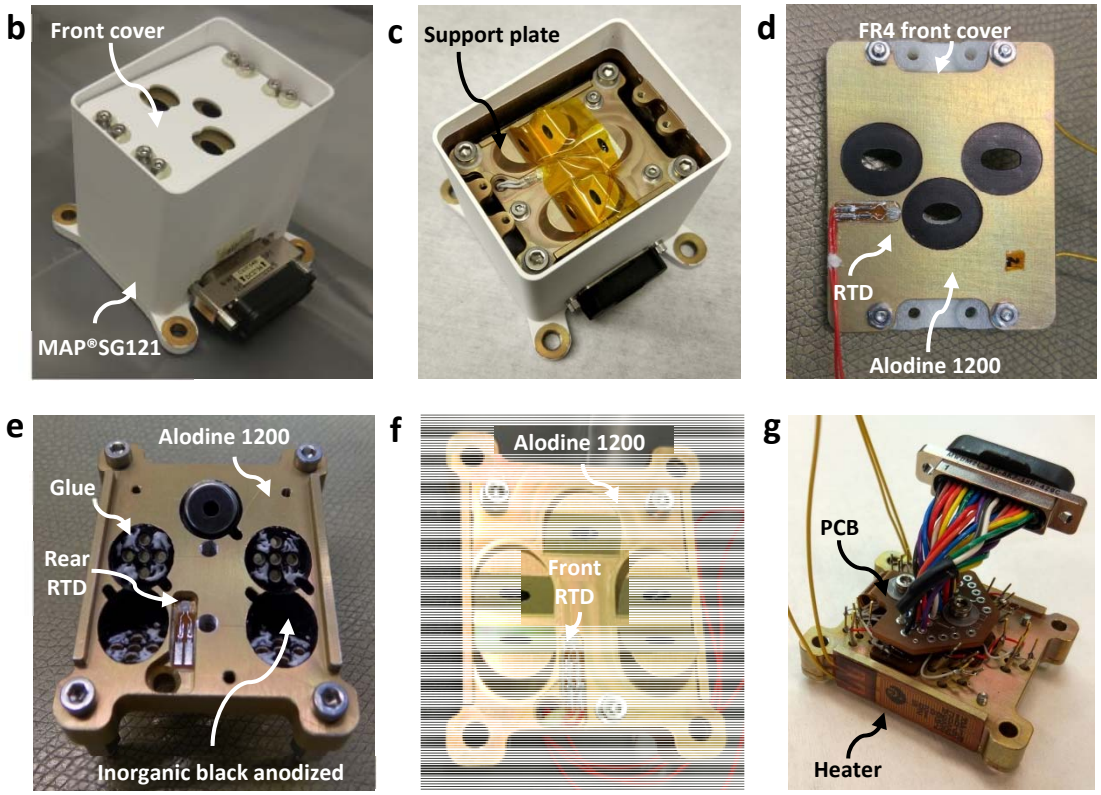

Figure 3. TIRS subassemblies, coatings and Resistance Temperature Detectors (RTD) locations (a) 3D design drawing and FoVs, (b) The housing and front cover, (c) Internal location of the support plate, (d) The calibration plate, (e) The support plate rear piece while gluing the thermopiles, (f) The support plate front piece subassembly, (g) The support plate printed circuit board (PCB) and electrical connections.

3. Radiometer mathematical model

(Eq. 1) shows the simplified mathematical model of all TIRS' channels already presented in [12]. The first term on the right-hand side (see Table 2 for the nomenclature) represents the net radiative flux exchange with the thermopile external elements, target, and calibration and

support plates (Fig. 4a), through their corresponding view factors. The second term on the right- accounts for the thermopile package inner flux exchange (Fig. 4b), and it represents the effect of package thermal gradients ($T_{sf} - T_s$) calculated using the Stefan-Boltzmann law because there is no filter limiting the bandpass of the fluxes inside the thermopile. Given the operational temperatures, the IR flux leaving and coming from the support and calibration plates for a thermopile with a quartz filter (channel IR3) can be neglected, $\varphi_{cp} \sim \varphi_{sp} \sim \varphi_s \sim 0$ [6]. Therefore, (Eq. 1.1) can be rewritten into (Eq. 1.2) for this channel.

$$V_{out} = S(T_s) \cdot A_s \cdot \left(F_{s-t} \cdot \varphi_t + F_{s-cp} \cdot \varphi_{cp} + F_{s-sp} \cdot \varphi_{sp} - \left(F_{s-t} + F_{s-cp} + F_{s-sp}\right) \cdot \varphi_s\right) + S(T_s) \cdot A_s \cdot \left(1 - F_{s-t} - F_{s-cp} - F_{s-sp}\right) \cdot \left(\sigma \cdot T_{sf}^4 - \sigma \cdot T_s^4\right) \quad (1.1)$$

$$V_{out} = S(T_s) \cdot A_s \cdot \left(F_{s-t} \cdot \varphi_t + \left(1 - F_{s-t} - F_{s-cp} - F_{s-sp}\right) \cdot \left(\sigma \cdot T_{sf}^4 - \sigma \cdot T_s^4\right)\right) \quad (1.2)$$

Table 2. Nomenclature.

Parameter		**Nominal values / error 1σ**
V_{out}	thermopile voltage, V	
$S(T_s)$	thermopile responsivity versus temperature, V/W	
A_s	thermopile detector area, m^2	1mm^2
F_{s-sp}	thermopile detector-support plate view factor	~ 0.1815
F_{s-cp}	thermopile detector-calibration plate view factor	~ 0.0335
F_{s-t}	thermopile detector-target view factor	~ 0.0410
F_{t-sh}	target-chamber sample holder and TIRS view factor	~ 0.17±0.08
ε_t	target emissivity of the calibration set-up	0.91±0.015
φ_t	target radiosity (emitted plus reflected) inside channel spectrum, W/m^2	
φ_{cp}	calibration plate radiosity (emitted plus reflected) inside channel spectrum, W/m^2	
φ_{sp}	support plate radiosity (emitted plus reflected) inside channel spectrum, W/m^2	
φ_s	thermopile detector radiosity (emitted plus reflected) inside channel spectrum, W/m^2	
T_t	Target temperature, K	
T_s	thermopile detector temperature reference, K	
T_{sf}	thermopile detector temperature (housing front part), K	
$T_{sp\text{-}f}$	support plate front temperature (front piece), K	
T_{sp}	support plate temperature (rear piece), K	
T_{cp}	calibration plate temperature, K	
T_{sh}	chamber sample holder temperature, K	
σ	Stefan-Boltzmann constant, W/m^2· K^4	
K, *h*, *c*	Planck's law constants	
$\chi(\lambda)$	thermopile spectral response versus wavelength	
λ	*w*avelength, m	

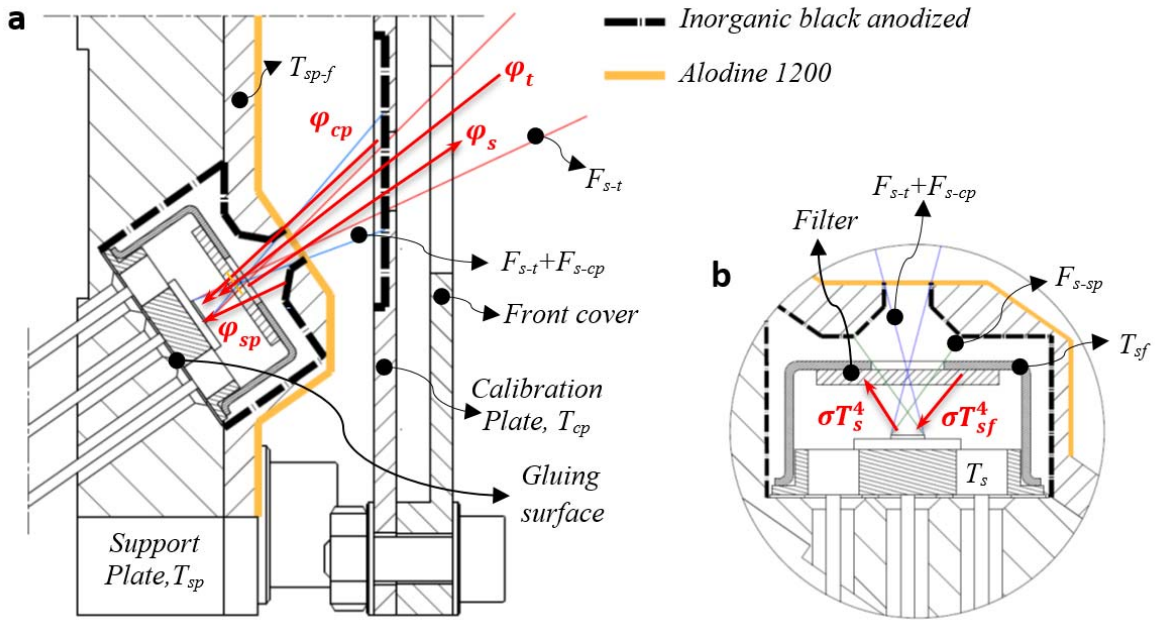

Figure 4. (a) Thermopiles external IR flux diagram and temperatures, (a) Thermopiles internal IR flux diagram and temperatures.

The thermopiles' thermal gradient ($T_{sf} - T_s$) cannot be directly measured because of their small value and the small size of the package, and therefore they need to be estimated. This is the main objective of the thermal calibration described in this article. The themopiles' responsivity, view factors, and the detector area are known terms whose values have been previously defined or subjected to radiometric and angular calibration. Their nominal and experimental values for each channel are provided in (Table 2) and [12].

The radiosity terms for the target, detector and support plate for each channel are calculated using Planck's law [12]. The expression for the calibration target has been particularized for the calibration setup in section 5. The expressions for support plate and detector are shown in Eqs. 2.1 and 2.2. Note that a value of 1 for the support plate emissivity was considered, as it is forming an almost close cavity with the thermopile package, and it is coated with a high emissivity inorganic black anodized treatment[12]. Also, the emissivity of the detector is assumed to take a value of 1 inside the channel bandpass because the sensing element emissivity is equal to its absorptance, and its effect is already included in the channel spectral response. The calibration plate radiosity calculus is more complex because of the appearance of multiple reflections, and its mathematical expression can be found in [12].

$$\varphi_s = \int_0^\infty \chi(\lambda) \frac{2\pi hc^2}{\lambda^5\left(e^{hc/\lambda K T_s} - 1\right)} d\lambda \tag{2.1}$$

$$\varphi_{sp} = \int_0^\infty \chi(\lambda) \frac{2\pi hc^2}{\lambda^5\left(e^{hc/\lambda K T_{sp\_f}} - 1\right)} d\lambda \tag{2.2}$$

4. Thermal mathematical model (TMM)

Thermopiles packages' thermal gradients cannot be completely eliminated by the TIRS thermo-mechanical design. This is because the TIRS calibration and support plates, as well as its external housing, are thermally coupled to the Martian environment, and at the same time to the thermopiles' package. Therefore, the thermal loads and artifacts of the Martian environment

result in a thermal flux between the TIRS external housing and the thermopiles, generating thermal gradients between the front and the rear elements of the thermopiles' packages [12]. Moreover, when the support and/or calibration plate heaters are activated during in-flight calibration operational mode, additional thermal gradients will appear.

Since this thermal environment is very difficult and costly to recreate inside a simulation chamber, here we use the TIRS's TMM [13] to: i) estimate the thermopiles' package spatial thermal gradients and their correlation using estimative quantities, ii) extend the validity of the calibration test results to the different operational scenarios (temperature range, wind and solar loads), and iii) help define of the accuracy of the thermal gradient estimators.

The TIRS's TMM is based on geometrical mathematical models and use the software tool ESATAN-TMS r7 released in 2017. The TMM consists of 823 thermal nodes, 820 of which are shell nodes (3D geometrical finite elements) and 3 are non-geometrical nodes (external and internal atmosphere finite elements). The nodes represent the conductive and radiative boundaries of the instrument. Radiative calculations have been performed with Monte Carlo Ray Tracing. Internal conductive couplings have been calculated considering the thermal contact resistance. Convection has also been considered for small internal cavities, where the effects of the Martian atmosphere are not negligible. The TMM has been completed with the addition of the solar loads, the convective exchange factor calculation, and the boundary conditions. In addition, a reduced model of the NASA Mars 2020 rover has been used to represent the radiative environment of the instrument with a higher fidelity, including the effect of the shade produced by the rover, which can be an important factor for the gradients, due to the sudden change in solar loads. The rover yaw angle has been selected to represent a worst orientation for each case. The orientation that produces maximum solar irradiation during all the day has been applied for the hottest day (except when it is shadowed by the rover). On the other hand, the selected orientation for the coldest day leads to the instrument to be protected from solar irradiation during most of the time. The analyzed scenarios are the diurnal cycle for the simulated coldest day or WCC (worst cold case), and hottest day or WHC (worst hot case). These two extreme cases cover the whole range of temperature conditions the instrument will encounter, ensuring the existence of changes in the solar load seen by the TIRS.

The need to verify the thermal gradients of the thermopiles package leads to a detailed representation with higher discretization in the number of thermal nodes of the thermopile surrounding elements, despite the high thermal conductivity of those components made of aluminum (Fig. 5). The package of the thermopiles has been modeled by two thermal nodes, one at the front and the other at the rear, with the aim of evaluating the thermal gradient between the two. The thermal properties of the package material were defined according to the base material, polished stainless steel, with an IR emissivity of ~ 0.1 [12]. This represents a relevant simplification since the filter and its thermal properties have not been modeled.

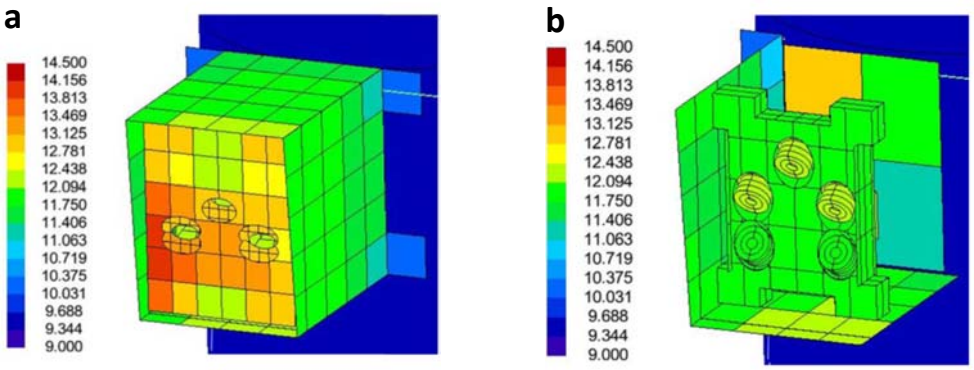

Figure 5. TIRS TMM temperature map results in Celsius for the WHC (Worst Hot Case) scenario and heaters OFF. (a) The front cover and housing, and b) the support plate and thermopiles.

Finally, to reduce uncertainty in the TMM results, some of the model parameters have been adjusted and correlated following the procedure described in [19], with the quasi-steady and transient results of dedicated tests. The parameters of the TMM that were modified during the correlation are five: The conductive couplings between TIRS housing and the support and calibration plates through the bolted joints and cabling, the conductive couplings between support plate and the thermopiles through gluing and cabling, and finally the thermopile housing thermal capacitance. The tests were performed in a simulation chamber recreating Martian atmospheric pressure and CO_2 composition. We employed a TIRS engineering model and three contact temperature sensors to monitor boundary conditions for chamber, mechanical interface and TIRS housing temperatures. The thermopile package thermal gradients were estimated using a quartz filter thermopile, IR3 channel, based on the simplified thermopile mathematical model for this channel (Eq. 1.2). The chamber was kept in dark conditions, $\varphi_t = 0$, so that thermopile voltage was only due to package gradients. The tests consisted of the activation of TIRS calibration and support plate heaters in different sequences, while temperatures were logged with a sampling rate of 90 sec. In the first test, calibration plate heater was power on during 1h with 0.8W, after that support plate heater was activated during 4 additional hours at maximum power, 0.8W. In the second test, the power of support plate heater was determined by the PI controller for four different support plate reference temperatures ~~references~~, that were changed every hour. The calibration plate heater remained off during this test. After TMM parameters fit, the correlation with experimental temperatures of the TIRS mechanical elements was better than 0.6K, while the correlation with the gradients in the thermopile package was better that 5mK.

4.1. Thermal model results

The TMM results for the temporal evolution of the thermopiles' package thermal gradients are presented here. (Fig. 6a) shows the evolution of the thermal gradients for channel IR3 under both scenarios, while (Fig. 6b) shows the same for the other channels under the WHC. Note that (Fig. 6b) shows no significant difference in the gradients of the different channels, which highlights the almost null effect of the thermopiles particular location and orientation. Additional cases where calibration and support plate heaters were dissipating 0.8 W during 30 and 50 min have been simulated. (Figs. 6c and 6d) show the results, with clear effects in the thermopile package gradients as a result of the driven power. In the case of the calibration plate heater activation (Fig. 6c), the generated gradient after the initial transient was positive during the heating (front part of the thermopile warmer than the rear). Conversely, the support plate heaters generate a negative gradient during the heating (Fig. 6d), which is compatible with the way the heat reaches the thermopiles from the rear part of the support plate.

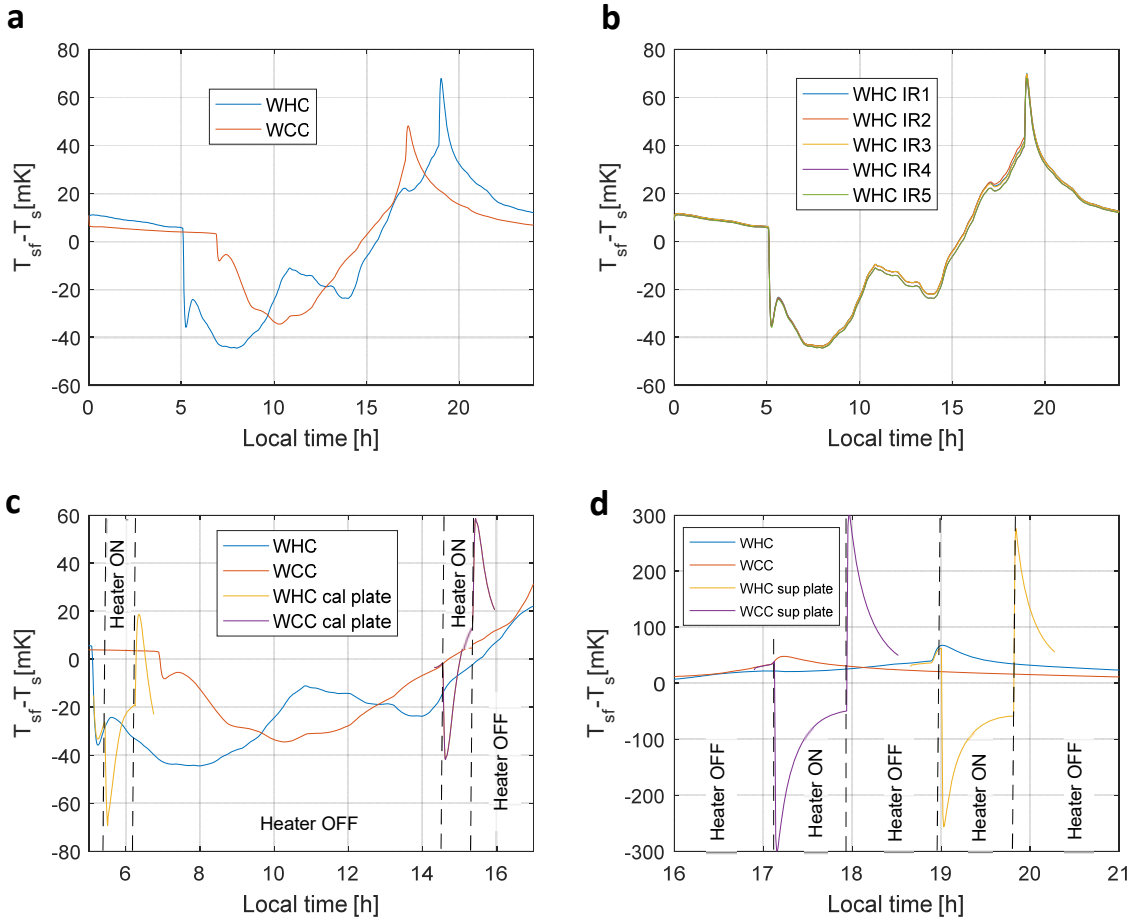

Figure 6. TMM results for thermal gradients between package front and rear. (a) Diurnal evolution of the IR3 channel for WHC and WCC scenarios, (b) Diurnal evolution of all channels for the WHC scenario, (c) The IR3 channel during calibration plate heating for WHC and WCC scenarios, (d) The IR3 channel during support plate heating for WHC and WCC scenarios.

A detailed analysis of the gradients during the diurnal WHC and WCC shows a high degree of correlation between the time derivative of the support plate temperature and the temperature gradient in the thermopile package, as shown in (Fig. 7a). Although not shown in this figure, this correlation works fine for the rest of the channels too. For each temperature time derivative, the temperature gradient in the thermopile package takes two slightly different values, due to the passage through said time derivative during the diurnal cycle increasing or decreasing the value of the derivative. Also, there is a difference between the WHC and WHC, that may be caused by the change in the model boundary conditions for both cases. These two effects shows that the gradients in the packages are also affected by other quantities, such as the existence of spatial gradients in the sensor structure (ex. between support and calibration plate), which are controlled by the external temperature evolution and solar loads. The effect of these spatial gradients between the calibration and the support plates can be seen in (Fig. 7b). Although the correlation is not as clear as in the case of the temporal derivative, a certain dependence may be observed.

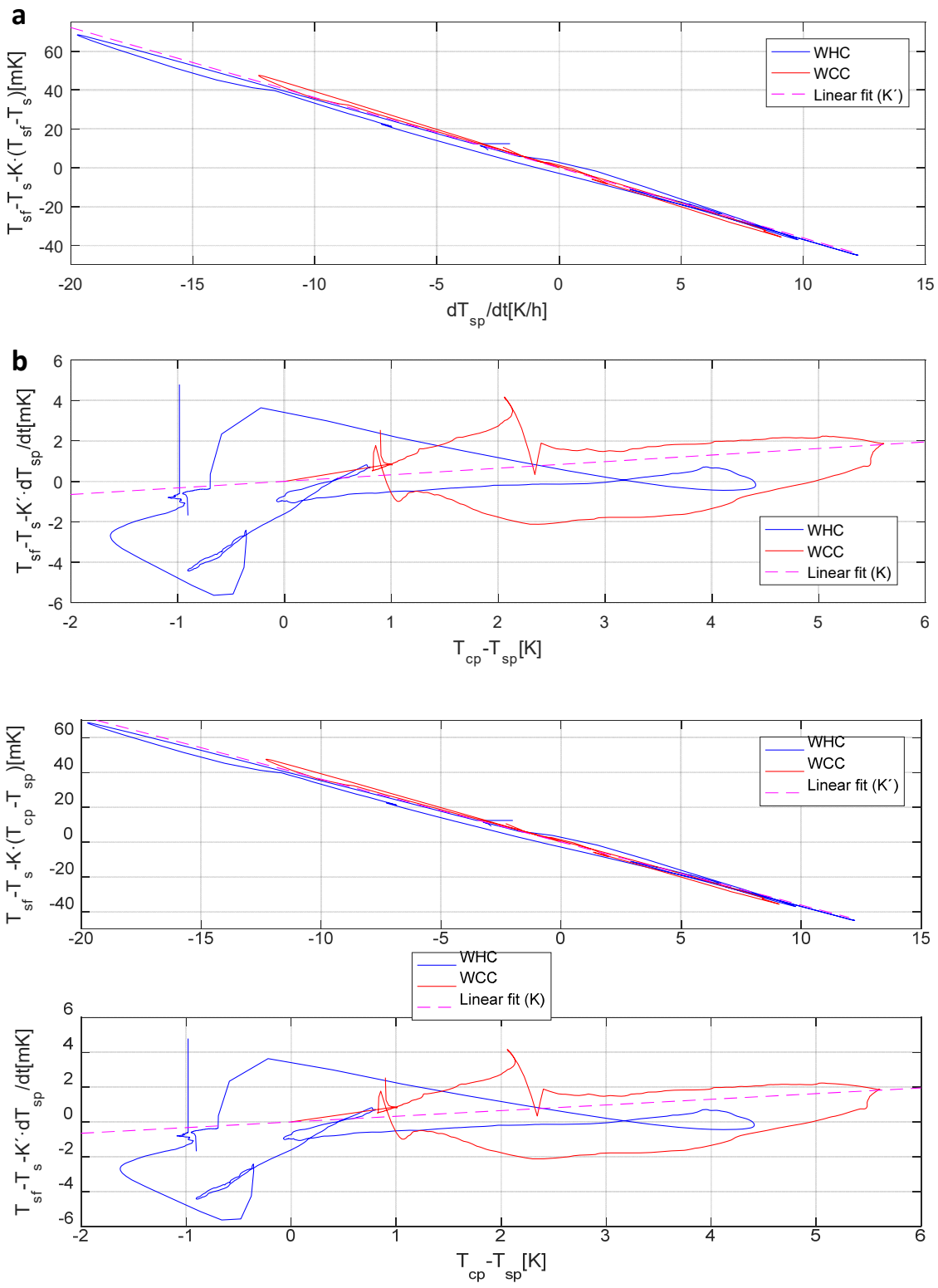

Figure 7. IR3 gradients analysis, (a) Correlation between support plate temperature time derivative and thermopile's package thermal gradient, (b) Correlation between calibration and support plates temperature difference and thermopile's package thermal gradient.

4.2 Thermopiles' thermal gradients estimators

Based on the results of the TMM, a set of mathematical equations has been defined as estimators to compensate for the thermopiles' thermal gradients effects. A similar compensation approach was already described in [8], where an empirical time dependence relation was established between the variation of the detector package temperature and the error induced in the detector output voltage. Also, in [10, 14, 18] a steady state relation between the power driven by the radiometer active thermal control system and the output voltage of the detectors was used with similar objectives. Contrary to these two approaches in which estimators compensate for the error output voltage of the detector, TIRS thermal estimators compensate for the package thermal gradients of the detector. This represents an advantage because this is the real mechanisms in which the error signal is generated, and therefore it is not affected by thermopile responsivity variation versus temperature. This allows for a simplification of the calibration setup and tested temperatures.

The design of the TIRS thermal gradient estimators accounts for operational modes. For nominal operation, the thermal gradients created by the diurnal temperature evolution and artifacts such as shadows and wind gusts are estimated using a linear and time dependent function shown in (Eq. 3.1). In this function, the thermopile spatial gradient is calculated from the temperature difference between the calibration and support plates, and the support plate temperature time derivative, through the constants *K* and *K'* respectively. The reason for selecting the spatial gradient between the support and calibration plates, instead of the gradient inside the support plate, which should be more related to the thermopiles' gradient, is that the former can be more easily measured because its value is higher and it is less affected by the resolution of the measuring electronics. (Fig. 7a and 7b) show the results of fitting of the proposed estimator for the data of the TMM (linear fit of *K* and *K'*). To graphically assess the fit, the y-axis of the figures has been modified to subtract the contribution of the other fitting term. The fit provides values of $K_{TMM} = 0.325\, mK/K$, $K'_{TMM} = -3.612\, mK/K \cdot h$, with standard errors of $\sigma_{K\_TMM} = 0.015\, mK/K$ and $\sigma_{K'\_TMM} = 0.005\, mK/K \cdot h$, representing error of 4.61% and 0.14% respectively, and a standard deviation of the misfit of 1.38 mK.

$$T_{sf} - T_s = K \cdot \left(T_{cp} - T_{sp}\right) + K' \cdot \partial T_{sp}/\partial t \tag{3.1}$$

$$T_{sf} - T_s = K_{cp0} + K_{cp1} \cdot \left(T_{cp} - T_{sp}\right) + K' \cdot \partial T_{sp}/\partial t \tag{3.2}$$

$$T_{sf} - T_s = K_{sp0} + K_{sp1} \cdot Power_{sp} + K_{sp2} \cdot \left(T_{cp} - T_{sp}\right) + K_{sp3} \cdot Power_{sp}{}^2 + K_{sp4} \cdot Power_{sp} \cdot \left(T_{cp} - T_{sp}\right) \tag{3.3}$$

Outside the nominal operations, in-flight calibration operation modes are also affected by thermal gradients in the thermopiles. For the in-flight calibration mode using the calibration plate, the calibration plate heating power is constant but the generated thermopile package's gradient during its activation is modified by external factors such as: the external thermal scenario, solar loads, and winds. Therefore, to take into account this fact the thermopile package gradients estimation function linearly depends on the spatial gradient between the calibration and support plates (Eq. 3.2). This spatial gradient has been selected because it is strongly affected by heater activation and depends on previously described external factors. The in-flight calibrations will be executed during the period of the Martian day when ambient and ground temperatures are more stable (ex. before sunrise or at noon). This will help to limit the support plate temperature time derivative, but without making its value null. Therefore, the time derivative of the support plate is also part of the estimator for this calibration mode (Eq. 3.2).

For the calibration mode using the support plate, a steady state function is defined (Eq. 3.3), because the support plate temperature is kept stable by the PI controller and the term depending on *K'* is not needed. The equation shows a two variables nonlinear function, assuming a polynomial of order 2 for power driven to the support plate heater since, in this case, heating power is modulated by the PI controller, and order 1 for the spatial gradient between the

support plate and the calibration plate. The spatial gradient between the calibration and support plates has been selected because of reasons like those exposed above. The independent term of the polynomial is assumed to take a null value, $K_{sp0} = 0$, since the gradients in the package must be null in the absence of power dissipated in the support plate. (Fig. 8) summarizes the thermal gradient calibration and compensation approach.

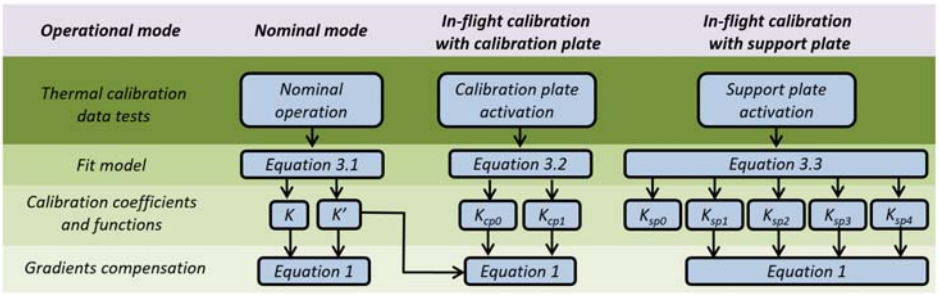

Figure 8. Thermal gradients estimation and compensation approach.

5. Thermal calibration tests

The TIRS thermal calibration plan includes a set of tests to identify the value of the constants and functions of the thermopiles' thermal gradients estimators appearing in Eqs. 3.1, 3.2 and 3.3.

5.1 Experimental setup

The MARTE simulation chamber [20], designed by the Centro de Astrobiología in Madrid (Spain), has been used as the main testing facility (Fig. 9a). This facility complies with the requirements and limitations imposed by the planetary protection plan of the mission. The Martian atmospheric composition and pressure is recreated inside the chamber, evacuate down to 10^{-3}mbar and then~~m~~ filling the chamber using as base gas a bottle of 100% of CO_2 till reaching 8mbars. The pressure is measured with a capacitive temperature compensated sensor model CMR 232 from Pfeifer GmbH.

The chamber allows the simulation of the gradient between the rover mast and the Martian atmosphere and its diurnal evolution. To this end, the TIRS was thermally coupled to chamber sampler holder. The sample holder has the capacity to generate temperature profiles within ±20K around room temperature, while the chamber walls remain at this room temperature. This is the main limitation of the setup, since it is not possible to cover the entire TIRS operational temperature range [13]. Another limitation is the inability to recreate the effects of wind gusts or solar loads, due to the difficulties to generate wind flow at Martian pressure and the influence of both effects in the temperature stability of the calibration target.

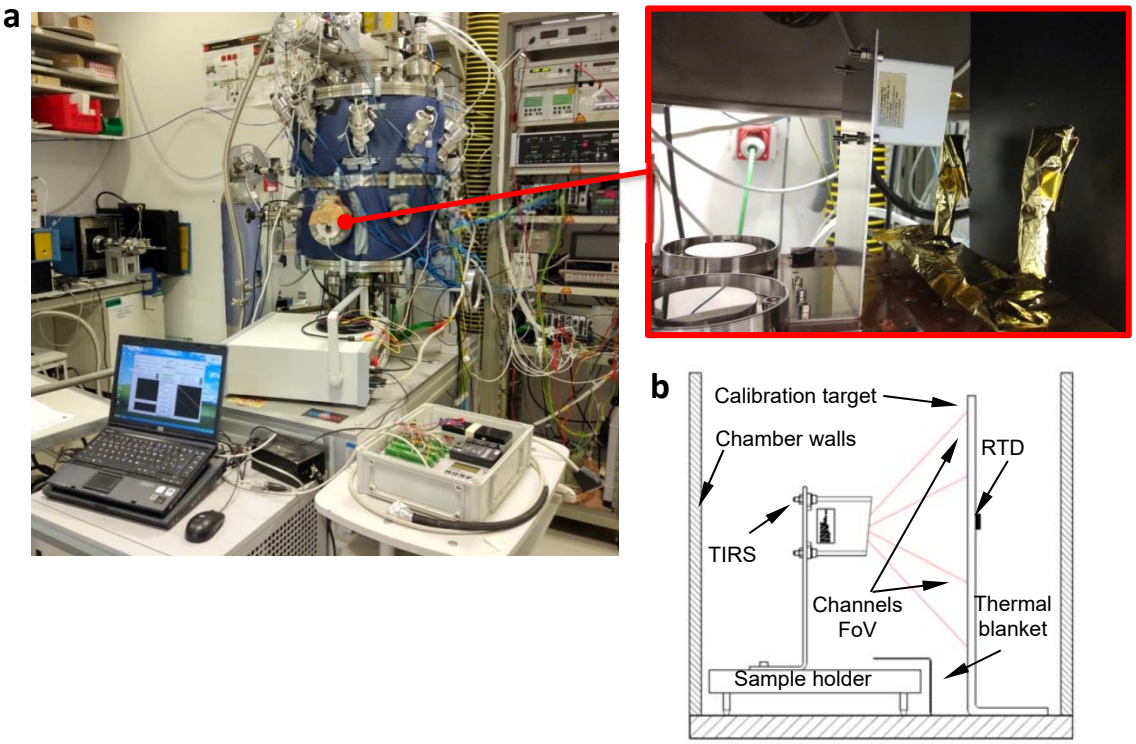

Figure 9. MARTE chamber test setup, (a) External and internal photos, (b) Simplified calibration diagram

Inside the chamber there is a calibration target formed by a copper plate painted with a high emissivity coating (Aeroglaze® Flat Black Absorptive Polyurethane with an average emissivity of ~0.91 in the range 5-35 μm) [21]. The target was thermally coupled to the chamber walls (Fig. 9b). Its temperature was not controlled but measured using a RTD glued to its surface. The chamber and the calibration target form a closed cavity at a similar temperature. Nevertheless, the chamber sample holder is awfully close to the calibration target and the changes in its temperature during the calibration generate reflections on its surface that modify the calibration target radiosity. To compensate for this effect, a simplified geometric model of the calibration setup has been implemented. The model allows for computing the radiosity of the calibration target φ_t by integrating Planck's law inside the channels' bandpass from the measured temperatures of the target and the sample holder, the emissivity of the target radiant surface and theoretical values of the vision factors between the focused surfaces of the calibration target and the walls of the chamber and the surface of the sample holder (Eq. 4). In the case of channel IR3, considering the bandpass of the quartz filter, the test is performed in dark conditions, $\varphi_t \sim 0$.

$$\varphi_t = \left(\varepsilon_t + (1-\varepsilon_t)\cdot(1-F_{t-sh})\right)\cdot\int_0^\infty \chi(\lambda)\frac{2\pi hc^2}{\lambda^5\left(e^{hc/\lambda KT_t}-1\right)}d\lambda + (1-\varepsilon_t)\cdot F_{t-sh}\cdot\int_0^\infty \chi(\lambda)\frac{2\pi hc^2}{\lambda^5\left(e^{hc/\lambda KT_{sh}-1}\right)}d\lambda \quad (4)$$

Nominal values for F_{t-sh} and ε_t, as well as their associated uncertainties, are taken from (Table 2). Target and chamber sample holder temperatures are logged during the tests. The associated temperature uncertainties are ±0.2 K (standard error) for the target, including RTD and target contact temperature inhomogeneity, and ±1 K for the chamber sample holder. The latter is larger because of the thermal gradients affecting the sample holder. This leads to an uncertainty in the target radiosity equivalent to ±0.3 K.

Electrical measurements such as the calibration target, the support and calibration plate temperatures, the thermopiles' voltages and the support plate heater current, were performed using a KEITHLEY 2700 multimeter and a KEITHLEY 7700 commutation matrix. The multimeter was configured to log the value for all the temperatures and voltages every 30 seconds. Each particular sample is calculated by averaging 100 readings and by using an analog filter to reject 50 Hz noise. The heater driver is made up of a constant 12 V power supply and a PWM~~power wide modulator~~ to control the driving voltage for the case of the support plate driver. The modulator duty cycle was adjusted to provide 0, 25, 50 and 100% of the maximum power. The power dissipated at the heaters is calculated by measuring the current passing through them, assuming the nominal value of heaters' resistance. The power estimation error is below 2.8%, negligible for calibration purposes and mainly determined by current measurement error and heater resistance tolerances.

5.2 Calibration tests results

The experimental thermal calibration consisted of two different sets of tests, recreating the nominal and the in-flight calibration operational modes (Table 3).

Test purpose	Target temperature [K]	Sample holder [K]	Support plate heater power [W]	Calibration plate heater power [W]	Test conditions
1. Nominal mode (K *and* K' identification)	~300	286, 293, 300, 307, 314 Profile: ±14K/h, ±7K/h	0	0	Mars atmosphere, 8 mbar
2. In-flight calibration modes (Heaters function identification)	~300	286, 293, 300, 307, 314	~0, 0.2, 0.4, 0.8	~0, 0.8	Mars atmosphere, 8 mbar

Table 3. TIRS thermal calibration tests and conditions

The test for the nominal mode was aimed to simulate the thermal environment on Mars, while measuring the evolution of the thermopiles' thermal gradients. It consisted of creating a profile with different temperatures in the chamber sample holder (Fig. 10a). The change in the sample holder temperature, together with a smooth evolution of the temperature of the chamber's inner atmosphere, simulate the existence of positive and negative temperature differences (±14K and ±7K) between the rover RSM and the Martian atmosphere and generates thermal gradients between support and calibration plates, $T_{cp} - T_{sp}$. The sample holder temporal gradients (14K/h and 7K/h) simulate the diurnal evolution and the change rate of support plate temperature, $\partial T_{sp}/\partial t$ (Fig. 10b). These figures have been taken from the results of the TMM, that includes expected Martian conditions and the effect of solar loads and wind gusts [13].

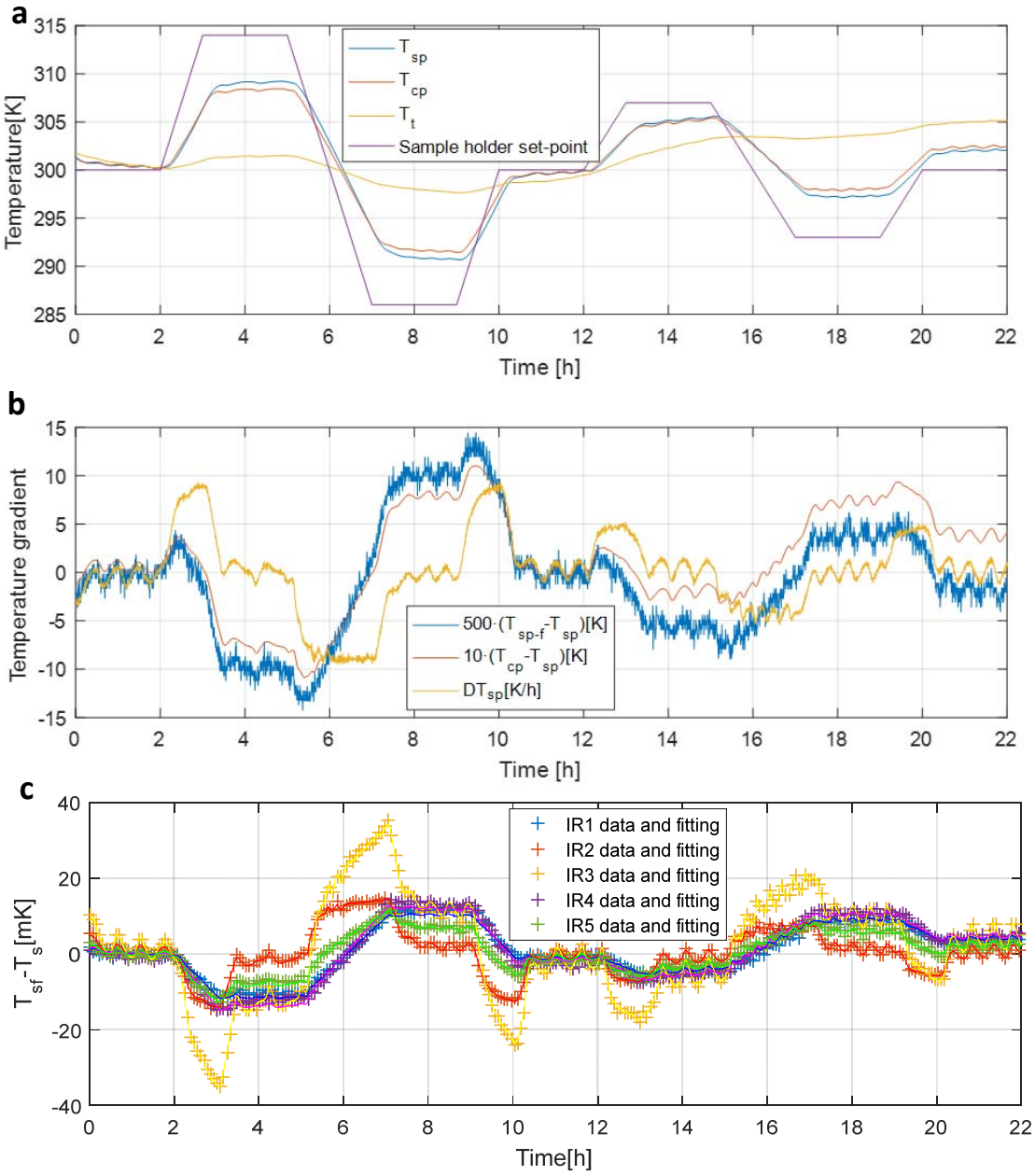

Figure 10. Nominal mode calibration test, (a) Chamber set point and TIRS temperatures profile, (b) Thermal gradients in TIRS subassemblies, (c) Thermopiles' package thermal gradient derived from (Eq. 5 and 5.2), decimated samples (+) and model fit (solid lines) derived from (Eq. 3.1).

Practical test results (Fig. 10b), show that the expected values for support plate time derivative has been partially achieved, with ±10K/h versus the +10Kh and -20K/h for the TMM, while the test was not capable of covering Martian range for $T_{cp} - T_{sp}$. Based on the results of the TMM $T_{cp} - T_{sp}$ should take values from -1.5K to +5.6K, while in the practical test is limited to ±1K. The main reason is the impossibility to recreate solar loads.

Measured data are introduced in (Eq. 1.1 and 1.2) together with the previously calibrated constant and terms of [12]. Then (Eq. 1.2) for channel IR3, and (Eq. 1.1) for the other channels are solved for T_{sf} , obtaining (Eq. 5.2 and 5.1) respectively. Finally, the evolution of the thermopile package gradient $(T_{sf} - T_s)$ is computed (Fig. 10c).

$$T_{sf} = \left(\frac{\left(\frac{V_{out}}{S(T_S)\cdot A_S} - F_{s-t}\cdot\varphi_t - F_{s-cp}\cdot\varphi_{cp} - F_{s-sp}\cdot\varphi_{sp} + \left(F_{s-t}+F_{s-cp}+F_{s-sp}\right)\cdot\varphi_s\right)}{\left(\left(1-F_{s-t}-F_{s-cp}-F_{s-sp}\right)\cdot\sigma\right)} + T_s^4 \right)^{1/4} \quad (5.1)$$

$$T_{sf} = \left(\frac{\left(\frac{V_{out}}{S(T_S)\cdot A_S} - F_{s-t}\cdot\varphi_t\right)}{\left(\left(1-F_{s-t}-F_{s-cp}-F_{s-sp}\right)\cdot\sigma\right)} + T_s^4 \right)^{1/4} \quad (5.2)$$

The experimental values obtained for the thermopiles' package gradients are different depending on the channel (Fig. 10c). For some channels, particularly IR2 and IR3, the gradients introduce important uncertainties, potentially compromising the accuracy requirements [6], and thus justifying the need for calibration presented in this article (Table 4). Equivalent target temperature or irradiance errors have been calculated assuming a nominal thermal environment [6], where ground temperature is equal to T_s -20K, sky temperature is T_s -70K and atmosphere temperature is T_s-10K.

Channel	Maximum gradient [mK]	Equivalent error T_s = 298K	Equivalent error T_s =173K
IR1	±12	±2.55W/m^2[a]	±2.37W/m^2[a]
IR2	±15	±13.77K	±13.44K
IR3	±35	±4.49W/m^2	±4.49W/m^2
IR4	±14	±2.72W/m^2[a]	±2.72W/m^2[a]
IR5	±11	±0.71K	±0.60K

[a] This error is calculated assuming a blackbody model for the target and Stefan-Boltzmann emission

Table 4. Nominal mode experimental values for package's gradients and equivalent target temperature or irradiance uncertainties without gradients compensation for two different thermopile package temperatures.

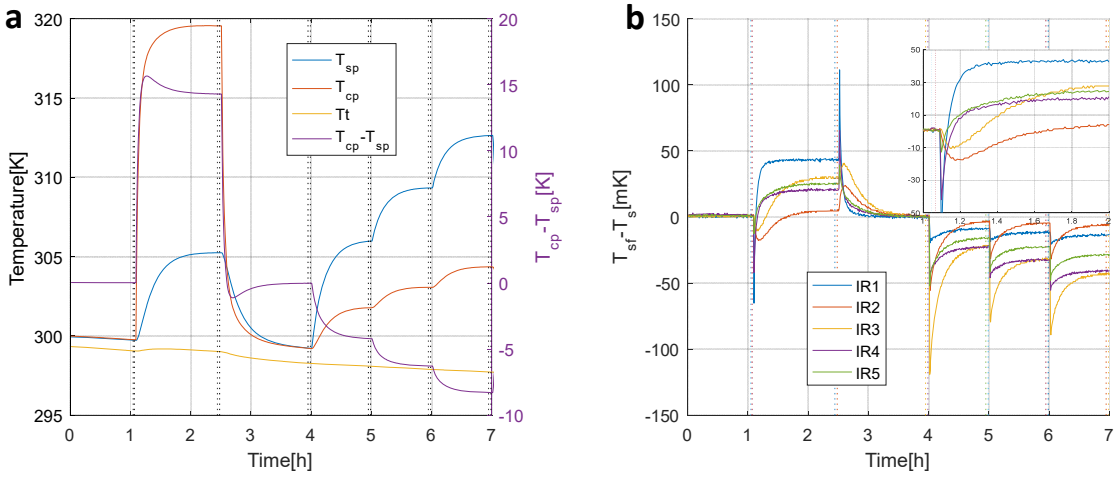

Figure 11. Thermopiles' package gradients results for in-flight calibration modes and chamber sample holder temperature of ~300K. (a) Temperature profiles vs. time during test development. (b) Thermopiles' package thermal gradients derived from (Eq. 5.1 and 5.2) vs. time, and (insert) zoom during calibration plate heating.

The aim of the second set of tests was to simulate the execution of the in-flight calibration algorithm either by driving power to the calibration plate or support plate, while measuring the evolution of the thermopiles' thermal gradients. The chamber sample holder temperature was set to different values (Table 3). For each temperature, a test sequence first drives power to the calibration plate during 1.5h, and then during 3h to the support plate with three different power levels: 25, 50 and 100% (Fig. 11a). A 1.5h of stabilization time is allowed between heater

activations to reach steady state conditions. Then, (Eq. 5.1 and 5.2) are solved, and then the thermopile gradient $(T_{sf} - T_s)$ is computed (Fig. 11b).

5.3 Estimators fit

Nominal mode test gradients were fit according to (Eq. 3.1) using a least square algorithm [22]. (Fig. 12) shows the results of the fit in the same way as for the TMM data. In this case, a clearer correlation with calibration and support plate temperature gradient is seen (Fig. 12b). The estimated coefficients, K and K', their standard error σ_K and $\sigma_{K'}$, and fit residuals are provided in (Table 5). (Fig. 10c) also shows the results of the fit (solid lines). The results of the different channels differ among them, but the results are consistent with the expected value, and largely coincided with the results of other models such as the Flight Spare (FS) and Bread Boards (BB and BB1).

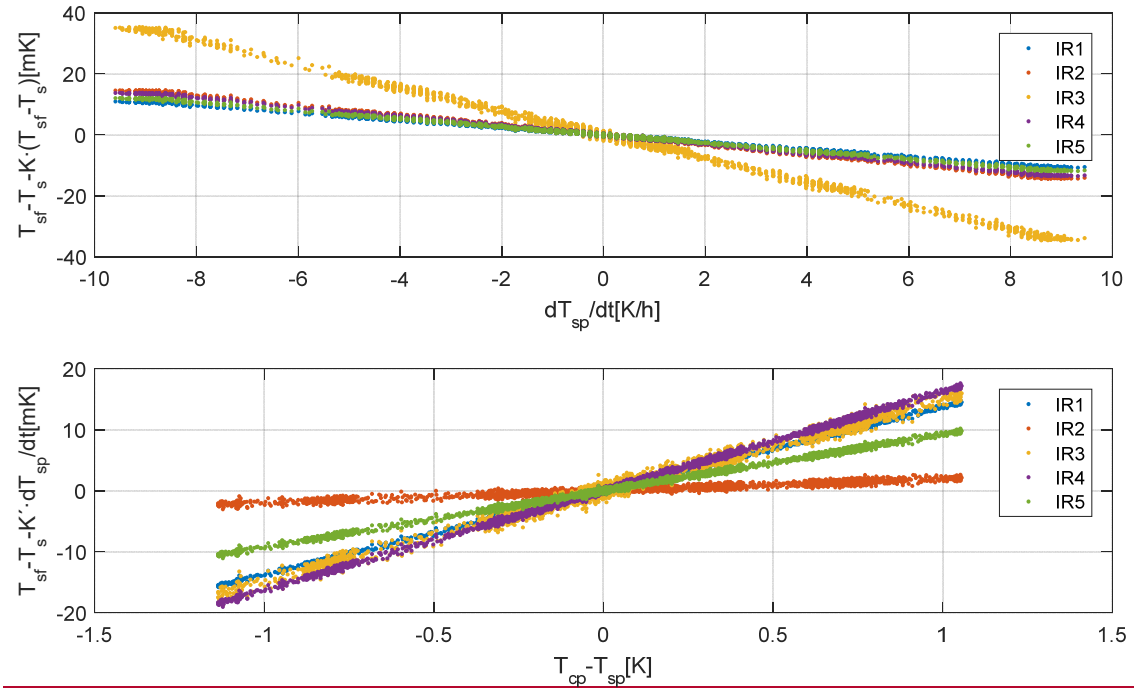

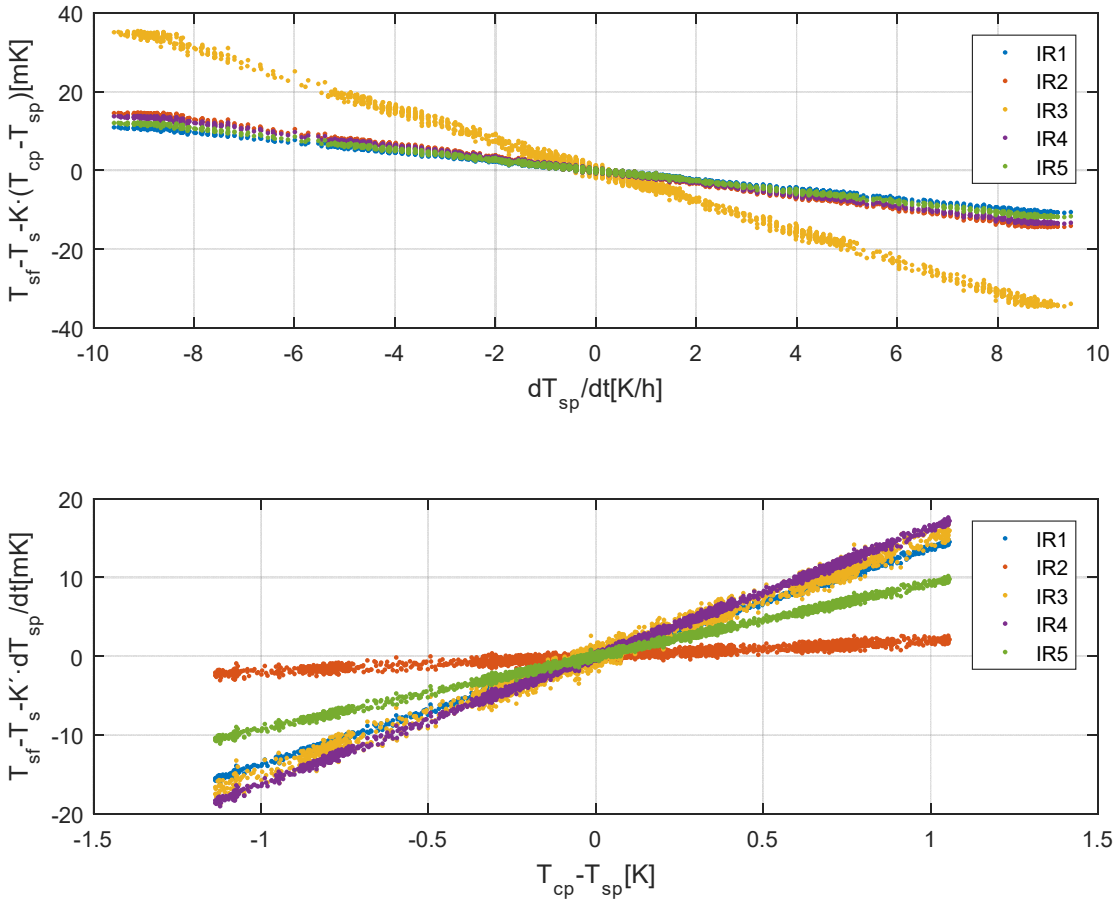

Figure 12. Nominal mode practical gradients analysis, (a) Correlation between support plate temperature derivative and thermopile's package thermal gradient ($\boldsymbol{K}'$ constant), (b) Correlation between calibration and support plates temperature difference and thermopile's package thermal gradient ($\boldsymbol{K}$ constant).

Channel	$\boldsymbol{K}$[mK/K]	σ_K [mK/K]	$\boldsymbol{K}'$[mK/K/h]	$\sigma_{K'}$ [mK/K/h]	Fit residual-1σ [mK]
IR1	13.70	0.0318	-1.205	0.0042	0.919
IR2	1.93	0.0095	-1.602	0.0012	0.438
IR3	14.91	0.0268	-3.861	0.0035	0.771
IR4	16.21	0.0322	-1.513	0.0042	0.929
IR5	9.21	0.0180	-1.326	0.0024	0.584

Table 5. Nominal mode gradient estimation coefficients (K and K'), associated estimation uncertainties (σ_K and $\sigma_{K'}$) and fit residuals

The test results for the calibration modes are summarized in (Fig. 13). For these modes only steady state gradients during calibration test development were considered, which are marked with vertical dotted lines in (Fig. 11a and b). (Fig. 13a) shows a compilation of the experimental values for the thermopiles' package gradients versus the spatial gradient between the support and calibration plates for all sample holder temperatures during the heating of the calibration plate. In addition, linear fits of the data for each channel [22], according to the gradients' estimation function of (Eq. 3.2), are plotted. Since this test uses data once the steady state regime has been reached, the term of (Eq. 3.2) depending on the temperature time derivative of the support plate takes a null value, and the associated coefficient cannot be identified. Thus,

the time derivative coefficient from (Eq. 3.1) is applicable for (Eq. 3.2) and the gradients compensation in this calibration mode. (Table 6) provides the coefficients of estimation polynomials and the fitting error. Standard errors for the coefficients have not been provided because of the small number of data (5 points) that leads to high and not real uncertainties. Fit residuals are compliant with target radiosity uncertainty.

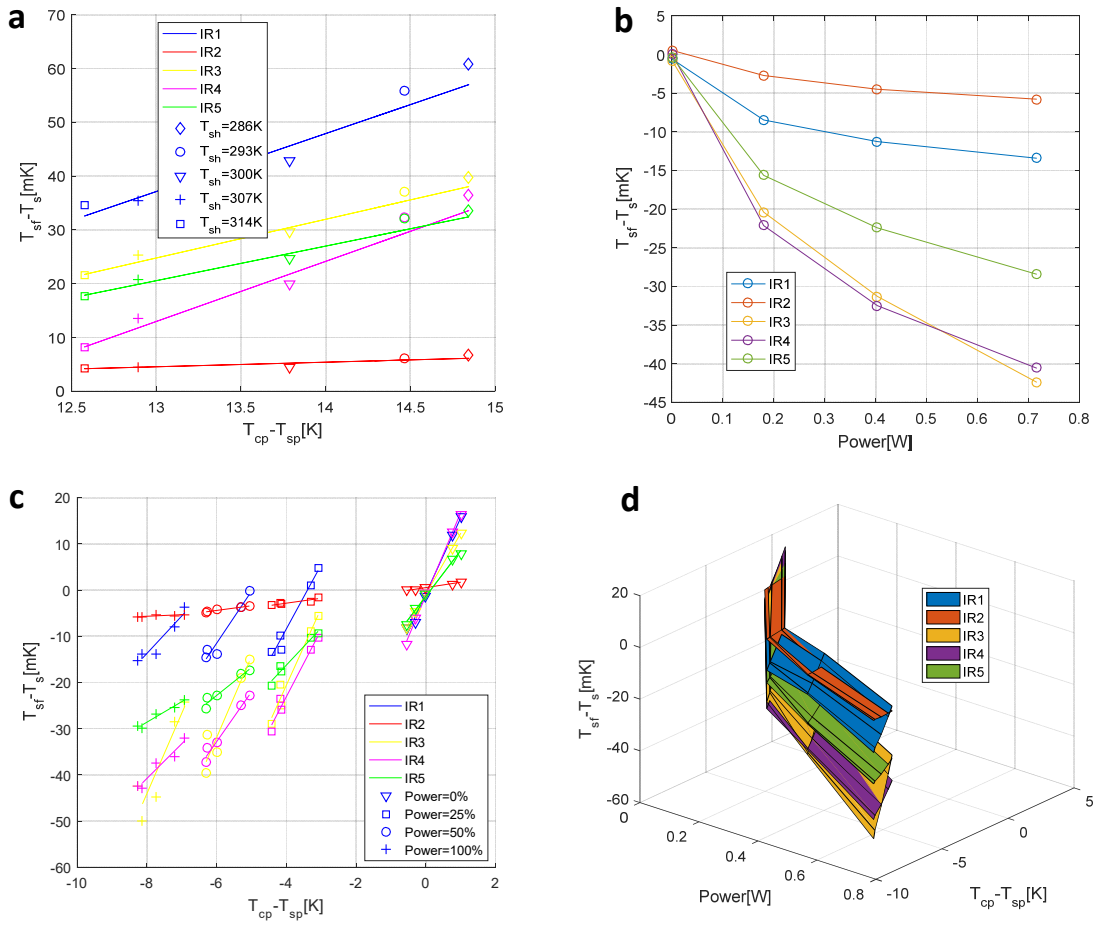

Figure 13. Thermopiles' package gradients results and fit for in flight calibration modes (a) Experimental data and linear estimation functions of the thermopiles' package gradients during the calibration using the calibration plate, (b) Experimental data of thermopiles' package thermal gradients versus heating power during the calibration using the support plate for a chamber sample holder temperature of ~300K, (c) Experimental data and linear estimation functions of thermopile's thermal gradients for the different heating powers during the calibration test using the support plate, (d) Polynomial surface estimation functions of thermopile's thermal gradients for the calibration mode using the support plate heater.

Channel	K_{cp0}[mK]	K_{cp1}[mK/K]	Fit residuals-1σ [mK]
IR1	-102.9	10.77	4.8
IR2	-6.5	0.85	0.66
IR3	-68.9	7.20	2.6
IR4	-132.3	11.17	4.3
IR5	-63.1	6.43	2.4

Table 6. Gradients estimator and fit residuals for the calibration mode using the calibration plate

(Fig. 13b) shows the quadratic dependence of the thermopiles' package gradients versus the heating power during support plate heating. (Fig. 13c) does the same for the linear dependence

of the package gradients versus the thermal gradient between the support and calibration plates for the different heating powers. Finally, (Fig. 13d) shows a 3D plot with the results of the global non-linear gradient estimation functions according to (Eq. 3.3). This function has been obtained by means of a polynomial adjustment using the Matlab® function *fit*, [22]. (Table 7) provides the coefficients of the non-linear gradient estimator and the fitting errors or residuals. Newly, residuals are compliant with target radiosity uncertainty, and standard errors for the coefficients have not been provided because of the small number of data (20 points) that leads to high and not real uncertainties. The non-zero and very small value for the independent terms, K_{sp0}, it is associated with an uncertainty in the temperature or irradiance of the calibration target, that leads to identify an unreal gradient in the thermopile package.

Channel	K_{sp0} [mK]	K_{sp1} [mK/W]	K_{sp2} [mK/K]	K_{sp3} [mK/W²]	K_{sp4} [mK/W·K]	Fit residuals-1σ [mK]
IR1	1.83	166.5	9.63	-95.1	1.85	4.1
IR2	0.60	1.3	1.03	-7.2	- 0.80	0.27
IR3	0.42	166.4	10.40	12.5	15.47	2.7
IR4	1.20	114.6	11.69	-105.6	-3.94	3.9
IR5	-0.20	55.6	6.82	-56.1	-2.56	2.0

Table 7. Gradient estimators and fit residuals for the calibration mode using the support plate

5.4 Discussion

The values of the obtained experimental thermal gradient for the IR3 channel, shown in Fig 10.c, coincide to a large extent with those predicted by the TMM, since the results of this type of thermopile for a different model were used in the adjustment of the TMM parameters and thus they are mathematically forced (section 4). This similarity is revealed mathematically in the values of K', $-3.612\, mK/K \cdot h$ for TMM versus $-3.861\, mK/K \cdot h$ for experimental of IR3 (Table 5). Nevertheless, for the other coefficient (*K*) of channel IR3 and for the rest of channels coefficients, experimental gradients differ significantly from the TMM results. Several factors justify these results:

i) First, the thermopile's filter covers a large part of the thermopile internal view factor (Fig. 4b) and factors such as filter optical properties (emissivity and reflectance) and the reflections inside the package are aspects that were not included in the thermopile's model, but that may affect the radiative exchange inside the package. Thus, the lack of filter modeling and the use of Stefan Boltzmann's law represent a clear simplification.

ii) Second, the differences in the thermal properties of the filter substrate, such us thermal conductivity, heat capacity and density and IR emissivity, modify the value and the temporal evolution of the gradients. (Table 8) shows the value of some of these quantities for the different substrate of the filters [23]. The thermal time constant of the filter, $\tau \sim c_p \cdot \rho/\lambda$, is directly proportional to the specific heat (c_p) and density (ρ) and inversely proportional to the thermal conductivity (λ). This implies that the quartz filter presents a time constant 8.5 times larger than germanium, and 22 times larger than silicon. This is consistent with the temporal responses shown in (Fig. 11b insert). On the other hand, the steady state thermal gradients between the filter (package front side) and the thermopile's package are inversely proportional to filter emissivity (ε) and the filter thermal conductivity (ρ). This dependence is clearly observed when we compare the value of the gradients between IR2 and IR3. Both filters present similar emissivity but a significantly different thermal conductivity, which implies a greater gradient in the case of IR3 given the lower thermal conductivity of the quartz. Similarly, IR5 and IR4 channels share Si as the filter substrate, and it is the lower emissivity of the IR4 channel filter that causes the greater gradient for this channel.

iii) Finally, another important aspect is related to the constructive details, both internal to each thermopile sample and external, such as its orientation and fixation to the support plate. One example is the amount of glue used and its distribution, both in the bonding of the filter and in the bonding of the thermopile to the support plate. This could explain the differences in the gradients for the case of channels with the same filter substrate but different orientation, as in the case of channels IR1 and IR4, as the TMM results do not justify any difference due upward or downward facing orientation (section 4.1).

Channel	Filter substrate	Emissivity (ε)	Thermal conductivity (λ)[a] ~@300K [W/K·m]	Specific heat (c_p)[a] ~@300K [J/K·Kg]	Density (ρ)[a] [Kg/m^3]
IR1 &IR4	Si	~0.53[b]	148	714	2330
IR5	Si	~0.7[b]	148	714	2330
IR2	Ge	~0.97[b]	59.9	320	5323
IR3	Quartz crystal	~0.93	12-6.8[c]	733	2650

[a] Assuming pure substances

[b] Based on filter transmittance (τ) data and assuming ε=1-τ for the filter high emissivity side

[c] Depending on the direction parallel or perpendicular to crystal *c* axis

Table 8. Thermal and optical properties of filter substrate

6. Thermal calibration performance and uncertainties

The results of the measurement errors for the different TIRS channels, before and after thermal gradients compensation for the calibration data set of the nominal mode, are presented in (Fig. 14). The errors are mainly associated to the thermopile's package thermal gradients and they are larger for channels IR2 and IR3 (Fig. 14a) because of their narrower bandpass filters and therefore their smaller signal-to-package's gradient ratio [15]. (Fig. 14b and 14c) show the excellent performance of the thermal estimators, reducing significatively the errors for channels IR2 and IR3 in a factor between 10 and 20, respectively. For channels IR1, IR4 and IR5 the improvement, although existing, is not so clear, being conditioned by errors in the radiosity of the calibration target. In addition to that, the compensation of the thermal gradients increases the associated noise because of the use of a derivative in the compensation (Eq. 3.1). The support plate temperature derivative has been computed using finite differences, in which a 6 samples moving average filter has been used to minimize the associated noise (sampling time 30 sec during calibration test). This allows a noise reduction of up to 0.33K (1σ) for IR2.

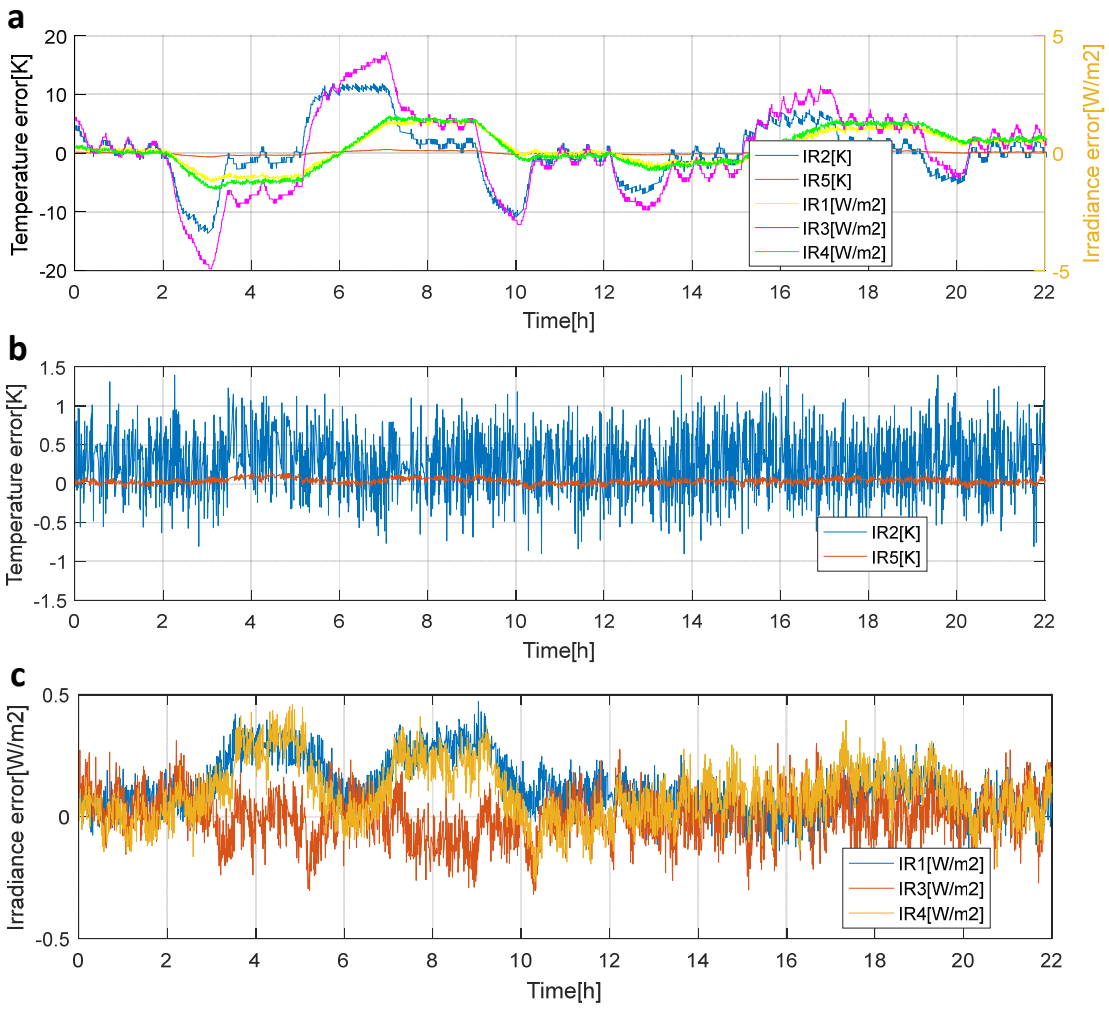

Figure 14. Target temperature or irradiance error for the different channels due to the thermopile package thermal gradients for the nominal operation calibration data set, (a) before applying thermal gradient compensation, and (b) temperature error after thermal gradient compensation, (c) irradiance error after thermal gradient compensation

The compensation of the thermopiles' package thermal gradients during nominal operations is affected by uncertainties, which originate from the following error sources:

(i) The limitations of the test setup, with respect to the inability to cover the entire operational temperature range and solar loads [13], affects the validity of the gradient estimation functions during Martian operations. To calculate the associated uncertainty, the TMM results has been used to extend the validity of the tests to different thermal environments. The TMM results for channel IR3 provide uncertainties for the estimation of K_{TMM} and K'_{TMM}, $\Delta K_{TMM} = \sigma_{K\_TMM}/K_{TMM} = 4.61\%$ and $\Delta K'_{TMM} = \sigma_{K'\_TMM}/K'_{TMM} = 0.14\%$ respectively. These two errors are propagated, taking partial derivatives in (Eq. 3.1) and adding quadratically the uncertainties. Thus, the uncertainty can be calculated according to (Eq. 6), where the values of $|T_{cp} - T_{sp}|_{max} = 5.6K$ and $|\partial T_{sp}/\partial t|_{max} = 20K/h$ are based on the results of the TMM, and K and K' are the coefficients for each channel result of the estimation form the calibration test (Table 5). The results are shown in (Table 9).

$$\Delta(T_{sf} - T_s) = \sqrt[2]{\left(K \cdot \Delta K_{TMM} \cdot |T_{cp} - T_{sp}|_{max}\right)^2 + \left(K' \cdot \Delta K'_{TMM} \cdot |\partial T_{sp}/\partial t|_{max}\right)^2} \quad (6)$$

(ii) The uncertainty in the determination of calibration target radiaosity, φ_t, equivalent to a calibration target temperature error of ±0.3 K. From the mathematical model of the

detectors (Eq. 1.1 and 1.2) an equivalent thermal gradient error can be computed using the real temperatures for target and TIRS during the test (Table 9). This error is very large for the channels IR1, IR4 and IR5, which should be reduced in future work.

(iii) The practical fit uncertainty of the gradient estimation functions. The procedure to calculate this uncertainty makes use of the standard errors of *K* and *K'* during its calibration (Table 5). The errors are propagated, taking partial derivative in Eq. 3.1 and using the maximum values for $|T_{cp} - T_{sp}|_{max}$ and $|\partial T_{sp}/\partial t|_{max}$ taken from the TMM. (Eq. 7) summarizes the procedure, and results for each channel are shown in (Table 9).

$$\Delta(T_{sf} - T_s) = \sqrt[2]{\left(\sigma_K \cdot |T_{cp} - T_{sp}|_{max}\right)^2 + \left(\sigma_{K'} \cdot |\partial T_{sp}/\partial t|_{max}\right)^2} \quad (7)$$

Channel	Testing temperature limitations (σ) [mK]	Calibration target equivalent temperature error (σ) [mK]	Gradients estimators (σ) [mK]
IR1	3.54	9.13	0.17
IR2	0.50	0.358	0.06
IR3	3.85	0	0.17
IR4	4.19	9.27	0.20
IR5	2.38	5.73	0.11

Table 9. Thermal calibration uncertainties expressed in terms of equivalent thermopiles' package thermal gradients errors.

Finally, Table 10 summarizes the total calibration uncertainty for the nominal mode of operation, and the equivalent target temperature or irradiance uncertainty. They have been calculated for extreme operational temperatures and a nominal thermal environment [6], where ground temperature is equal to T_s -20K, sky temperature is T_s -70K and atmosphere temperature is T_s-10K. To compute these figures the quadratic addition of the different uncertainties sources was used, assuming uncorrelated probability distributions for all of them.

Channel	Total uncertainty (1σ) [mK]	Nominal mode (Equivalent uncertainty -1σ T_s=298K)	Nominal mode (Equivalent uncertainty -1σ T_s=~173K)
IR1	9.79	2.08W/m^2[a]	1.93W/m^2[a]
IR2	0.62	0.55K	0.54K
IR3	3.85	0.49W/m^2	0.49W/m^2
IR4	10.17	1.98W/m^2[a]	1.98W/m^2[a]
IR5	6.21	0.40K	0.34K

[a] This error is calculated assuming a blackbody model for the target and Stefan-Boltzmann emission

Table 10. Thermal gradient total uncertainty and equivalent target temperature or irradiance uncertainty for two different detector temperatures

In-flight calibration is a differential process aimed at eliminating constant uncertainties by comparing measurements before and during the activation of TIRS heaters [6, 17]. Under this premise, a basic and preliminary analysis of the uncertainty associated with the calibration of the thermal gradients during the in-flight calibration modes can be carried out. In this analysis, it has been assumed that the fit residuals of the practical tests (Tables 6 and 7) correspond to the uncertainty value in the compensation of the thermal gradients, as no errors were identified for each of the estimator constants. By using the sensor model (Eq. 1), the fit residuals of the thermal gradients can be transformed into an equivalent error in the temperature of the calibration or support plates, depending on the calibration mode (Table 11).

Since the expected heating of the calibration plate during the in-flight calibration is around 15K (Fig. 11a), the equivalent temperature errors associated with the uncertainty in the gradient compensation (Table 11) take values between 1.1% and 3.5% of the temperature increment.

Similarly, a temperature increment of around 7K for the heating of the support plate is expected (Fig. 11a), with resulting associated errors between 0.9% and 1.6%. These uncertainties are compatible with the expected performance of the in-flight calibration system in the reevaluation of the detector responsivity, established at 3% in (Table 3) of reference [6]. As future work, a more exhaustive analysis of the performance of the flight calibration modes will be performed by means of an end to end test, making use of the gradient estimators obtained in this article.

Channel	Calibration plate equivalent temperature error (σ) [K]	Support plate equivalent temperature error (σ) [K]
IR1	0.22	0.08
IR2	0.52	0.11
IR3 [a]	-	-
IR4	0.20	0.08
IR5	0.16	0.06

[a] Channel IR3 cannot be recalibrated using in-flight calibrations [6, 12]

Table 11. Equivalent calibration or support plate temperature error for the calibration modes

7. Conclusions

The thermal gradients in the package of the IR detectors of Mars 2020 MEDA/TIRS instrument affects its accuracy, making it necessary to compensate for their effects. This is particularly the case for detectors with reduced spectral bandwidth such as channels IR2 and IR3. The thermal calibration approach makes uses of a simplified mathematical model [12] that accounts for such thermal gradients. Moreover, a set of time dependence and steady state equations for gradient estimation and compensation was defined, considering the different operational modes of TIRS.

TIRS TMM results have been used in the definition of the estimators, showing a high degree of correlation between the thermopiles' package spatial gradients and: (i) the temperature change rate experienced by the support plate where they are allocated, (ii) the spatial gradient between the support and calibration plate, and (iii) the power driven to the calibration heaters.

Calibration tests were performed to identify the coefficients of the functions for the estimation of the gradients. The results of the tests show important differences in the values of the gradients for the different types of thermopiles. This highlights, on the one hand, the simplification imposed by the mathematical modeling, and on the other, the effect of the IR filter material and its mounting in the value of the gradients.

The factors affecting the thermal calibration accuracy for the nominal operational mode were identified and assessed. These factors are: (i) The standard errors in the coefficients of the gradients estimation functions, (ii) the calibration target temperature accuracy, and (iii) the simplifications that the calibration setup imposes regarding operational temperature. For this last factor, the TMM results were used to estimate an upper bound for the error caused by the use of our experimental setup, since the test was performed at a unique temperature.

The thermal calibration resulted in a significant improvement in the TIRS performance and accuracy for channels IR2 and IR3 in the nominal mode, versus an approach in which thermal gradients are not compensated, and it allows carry out the in-flight calibration with the expected performance. The total uncertainty associated with the thermal calibration of the different channels range from 0.62 to 10.17mK, improving the 22 mK obtained in [6] as a preliminary value for all the TIRS channels. These numbers can be improved using a better calibration setup that reduce the uncertainty in the radiosity of the calibration target [10]. However, the current uncertainties meet the scientific requirements of the radiometer established by the Mars 2020 science team (<1% of irradiance and 5K in temperature) [6], validating the thermal calibration approach.

Funding: Instituto Nacional de Técnica Aeroespacial (INTA), Plan Estatal de I+D+I [ESP2014-54256-C4-1-R, ESP2015-68281-C4-1-R, ESP2016-79612-C3-1-R, RTI2018-099825-B-C31 and MDM-2017-0737], CDTI, USRA Contract Number 1638782, and LPI Contribution No 2369 (LPI is operated by USRA under a cooperative agreement with the Science Mission Directorate of the National Aeronautics and Space Administration).

Acknowledgment: This work forms part of the research project on the design and scientific issues of the NASA MARS2020 MEDA. A special thanks to all MEDA Co-Is and collaborators, who participated in a variety of ways in the development of MEDA TIRS, as well as reviewers for their contributions to the improvement of the article.

References

[1]. Farley, K. A., K. H. Williford, K. M. Stack, R. Bhartia, A. Chen, M. de la Torre-Juarez, K. Hand, Y. Goreva, C. D. K. Herd, R. Hueso, Y. Liu, J. N. Maki, G. M. Martínez, R. C. Moeller, A. Nelessen, C. E. Newman, D. Nunes, A. Ponce, N. Spanovich, P. A. Willis, L. W. Beegle, J. F. Bell III, A. J. Brown, S.-E. Hamran, J. A. Hurowitz, S. Maurice, D. A. Paige, J. A. Rodriguez-Manfredi, M. Schulte, and R. C. Wiens, Mars 2020 Mission Overview, Spa. Sci. Rev. (under review), 2020.

[2] Rodriguez-Manfredi, J. A., A. Alonso, V. Apestigue, I. Arruego, D. Banfield, J. Boland, J. Ceballos, A. Cobos, P. Conrad, E. Cordoba, T. del Rio, M. Dominguez-Pumar, S. Espejo, A. Fernandez, R. Ferrandiz, E. Fischer, M. Genzer, J. Gomez-Elvira, F. Gomez-Gomez, A.-M. Harri, C. Hernandez, M. Hieta, R. Hueso, J. J. Jimenez, V. Jimenez , A. Larman, A. Lepinette, M. Lemmon, S. Madsen, T. Mäkinen, M. Marin, J. Martín Soler, G. M. Martínez, A. Molina, L. Mora, J. Moreno, S. Navarro, C.E. Newman, C. Ortega, V. Peinado, A. Peña, I. Perez-Grande, S. Perez-Hoyos, J. Pla, J. Polkko, O. Prieto, M. Ramos, J. Romeral, A. Saiz-Lopez, A. Sanchez-Lavega, I. Sard, J.T. Schofield, E. Sebastian, M. D. Smith, R.E. Sullivan, L. K. Tamppari, A. Thomson, F. Torrero, J. Torres, R. Urqui, T. Velasco, D. Viudez-Moreiras and M. de la Torre Juarez, MEDA: The Mars Environmental Dynamics Analyzer. A suite of sensors for the Mars 2020 mission, Spa. Sci. Rev. (under review), 2020.

[3] Martínez, G. M., et al., The Modern Near-surface Martian Climate: A Review from In-situ Meteorological data from Viking to Curiosity, Space Sci. Rev., 212(1-2), 295-338, 2017.

[4] Banfield, Don, et al. "The atmosphere of Mars as observed by InSight." Nature Geoscience (2020): 1-9.

[5] Smith, Michael D. "Spacecraft observations of the Martian atmosphere." Annu. Rev. Earth Planet. Sci. 36 (2008): 191-219.

[6] J. Pérez-Izquierdo, E. Sebastián, G.M. Martínez, A. Bravo, M. Ramos, J.A. Rodríguez Manfredi, The Thermal Infrared Sensor (TIRS) of the Mars Environmental Dynamics Analyzer (MEDA) instrument onboard Mars 2020, a general description and performance analysis, Measurement, 122 (2018) 432-442. https://doi.org/10.1016/j.measurement.2017.12.004.

[7] M. Liess, A. Charlebois, M. Hausner, H. Ernst, H. Kragözoglu, J. Schilz, Stabilization of the output signal of thermopile sensors in the thermal environment of automotive applications, Proceedings of SPIE Photonic Applications for Aerospace, Transportation and Harsh Environments 6379 (2006).

[8] F.J. Meca, M. Mazo, F.J. Rodríguez, P. Ramos, Infrared temperature measurement system using photoconductive PbSe sensors without radiation chopping, Sens. Actuator A-Phys 100 (2002) 206–213. https://doi.org/10.1016/S0924-4247(02)00069-9

[9] M. Liess, H. Kragözoglu, H. Ernst, Reducing thermal transient induced errors in thermopile sensors in ear thermometer applications, Sens. Actuator A-Phys 154 (2009) 1–6. https://doi.org/10.1016/j.sna.2009.05.013

[10] Mueller, N. T., Knollenberg, J., Grott, M., Kopp, E., Walter, I., Krause, C., et al. (2020). Calibration of the HP^3 radiometer on InSight. *Earth and Space Science*, 7, e2020EA001086. https://doi.org/10.1029/2020EA001086

[11] Marquez, J.M.A.; Bohórquez, M.Á.M.; Garcia, J.M.; Nieto, F.J.A. A New Automatic System for Angular Measurement and Calibration in Radiometric Instruments. *Sensors* **2010**, *10*, 3703-3717.

[12] E. Sebastian, G.M. Martínez, M. Ramos, F. Haenschke, R. Ferrándiz, M. Fernández, J. A. Rodriguez Manfredi, Radiometric and angular calibration tests for the MEDA-TIRS radiometer onboard NASA's Mars 2020 mission, Measurement 164 (2020) 107968, https://doi.org/10.1016/j.measurement.2020.107968

[13] I. Perez-Grande, L. Peinado, A. Chamorro, I. Torralbo, G. Alonso, J. A. Rodriguez Manfredi, A. Lepinette and E. Sebastian, Thermal design of the Thermal InfraRed Sensor (TIRS) and the Air Temperature Sensor (ATS) of the Mars Environmental Dynamics Analyzer (MEDA) for Mars 2020, International Conference on Environmental Systems ICES 2017, Charleston, South Carolina, USA.

[14] M. Grott, J. Knollenberg, B. Borgs, F. Hänschke, E. Kessler, J. Helbert, A. Maturilli, N. Müller, The MASCOT radiometer MARA for the Hayabusa 2 mission, Space Sci. Rev. 208 (2017) 1-26. https://doi.org/10.1007/s11214-016-0272-1

[15] E. Sebastián, C. Armiens, J. Gómez-Elvira, Infrared temperature measurement uncertainty for unchopped thermopile in presence of case thermal gradients, Infrared Phys. Technol. 54 (2011) 75–83. https://doi.org/10.1016/j.infrared.2010.12.038

[16] Aslam, S., Amato, M. et al, Dual-telescope multi-channel thermal-infrared radiometer for outer planet fly-by missions Acta Astronautica 128 (2016)

[17] E. Sebastián, C. Armiens, J. Gómez-Elvira, M.P. Zorzano, J. Martinez-Frias, B. Esteban, M. Ramos, The Rover Environmental Monitoring Station Ground Temperature Sensor: A Pyrometer for Measuring Ground Temperature on Mars, Sensors, 10 (2010) 9211-9231. https://doi.org/10.3390/s101009211

[18] E. Kopp, N. Mueller, M. Grott, I.Walter, J. Knollenberg, F. Hanschke, E. Kessler, H.G. Meyer, HP3-RAD: a compact radiometer design with on-site calibration for *in-situ* exploration, Proc. SPIE 9973, Infrared Remote Sensing and Instrumentation XXIV, 2016.

[19] I. Torralbo, I. Perez-Grande, A. Sanz-Andres, J. Piqueras, Correlation of spacecraft thermal mathematical models to reference data, Acta Astronautica, 144, 2018

[20] J.M. Sobrado, J. Martín-Soler, J.A. Martín-Gago, Mimicking Mars: A vacuum simulation chamber for testing environmental instrumentation for Mars exploration, Rev Sci Instrum. 85 (2014), https://doi.org/10.1063/1.4868592

[21] M. Bass, et al., Handbook of Optics, Vol. 2: Devices, Measurements, and Properties, second ed., chap. 37, ISBN 0-07-047974-7.G.

[22] W.H. Press, S.A. Teukolsky, W.T. Vetterlin, B.P. Flannery, Numerical Recipes. The Art of Scientific Computing, third ed., Cambridge University Press, The Edinburgh Building, Cambridge CB2 8RU, UK, 2007. Chapter 15.2 and 15.4.4.

[23] David R. Lide, ed., *CRC Handbook of Chemistry and Physics, Internet Version 2005,* <http://www.hbcpnetbase.com>, CRC Press, Boca Raton, FL, 2005. Pages 2295-2310